

Efficient Bayesian inference using physics-informed invertible neural networks for inverse problems

Xiaofei Guan^{a,b}, Xintong Wang^a, Hao Wu^{c,a,*}

^a*School of Mathematical Sciences, Tongji University, Shanghai 200092, China*

^b*Key Laboratory of Advanced Civil Engineering Materials of Ministry of Education, Tongji University, Shanghai 200092, China*

^c*School of Mathematical Sciences, Institute of Natural Sciences, and MOE-LSC, Shanghai Jiaotong University, Shanghai 200240, China*

Abstract

In the paper, we propose a novel approach for solving Bayesian inverse problems with physics-informed invertible neural networks (PI-INN). The architecture of PI-INN consists of two sub-networks: an invertible neural network (INN) and a neural basis network (NB-Net). The invertible map between the parametric input and the INN output with the aid of NB-Net is constructed to provide a tractable estimation of the posterior distribution, which enables efficient sampling and accurate density evaluation. Furthermore, the loss function of PI-INN includes two components: a residual-based physics-informed loss term and a new independence loss term. The presented independence loss term can Gaussianize the random latent variables and ensure statistical independence between two parts of INN output by effectively utilizing the estimated density function. Several numerical experiments are presented to demonstrate the efficiency and accuracy of the proposed PI-INN, including inverse kinematics, inverse problems of the 1-d and 2-d diffusion equations, and seismic traveltime tomography.

Keywords: Bayesian inverse problems, Physics-informed deep learning, Invertible neural networks, Uncertainty quantification

1. Introduction

Inverse problems arise in various scientific and engineering fields, such as seismic tomography [1], material inspection [2], and medical imaging [3], etc. These problems aim to infer the input parameters of a system, such as physical fields, source locations, initial and boundary conditions, from the corresponding measurement data. However, inverse problems are typically ill-posed and difficult to solve because the measurement data originates from indirect sparse and noisy observations. It is of great practical value and theoretical significance to develop an efficient computation model for accurate and stable solutions, which has drawn much attention from scientists and engineers.

The classical approaches for inverse problems include the regularization methods and Bayesian inference. Regularization methods aim to find point estimates by simultaneously minimizing the misfits between observed data and solutions of forward problems with penalty functions [4, 5]. Bayesian inference incorporates uncertainties in prior information and observations by Bayesian rule and constructs the posterior distribution of the parameters, and therefore can effectively quantify the uncertainty of unknown input. However, in many applications, it is computationally expensive to sample from the intractable Bayesian posterior distributions by using statistical simulation techniques, e.g., Markov Chain Monte Carlo (MCMC)[6, 7, 8, 9], Hamiltonian Monte Carlo [10, 11], and Sequential Monte Carlo [12, 13]. To address these issues, many researchers utilized various variational inference algorithms to improve computational efficiency, including mean-field variational inference [14, 15], automatic differential variational inference[16, 17], and Stein variational gradient descent[16, 18]. But the variational methods may face challenges in high-dimensional settings due to the difficulty of accurately approximating posterior distributions with the tractable surrogate

*Corresponding Author

Email address: hwu81@sjtu.edu.cn (Hao Wu)

distribution. Although all aforementioned methods have shown to be relatively efficient, they still require numerous evaluations of the forward model and the complicated parametric derivatives. Consequently, deep learning-based methods offer an efficient alternative, where they are capable of providing real-time inversions for certain classes of inverse problems with new measurement data of similar type.

Deep learning methods have emerged as a promising approach for solving inverse problems, such as medical imaging [19, 20] and electromagnetic inversion [21, 22]. Nevertheless, these methods heavily rely on labeled data from solutions of the forward problem, rendering them inappropriate for inverse problems where such information is not present. Then, Raissi et al. [23] proposed the physics-informed neural network (PINN), which can utilize the information of physical equations instead of labeled data to solve partial differential equations (PDEs). Enormous related research has shown that PINN can also efficiently recover the unknown parameters [24, 25, 26, 27, 28, 29, 30, 31, 32]. In addition, deep generative models have made significant progress in the machine learning community, including generative adversarial networks (GANs) [33], variational autoencoders (VAEs) [34], and invertible neural network (INN) based models [35, 36, 37]. INNs have gained significant attention, particularly for their efficiency and accuracy advantages in both sampling and density estimation of the complex target distribution through a bijective transformation. This approach has shown potential in Bayesian inference [38, 39, 40, 41, 42]. However, there are still some limitations in current works. For instance, INN models [38, 39, 40] require significant amounts of labeled data for pretraining, which is often unavailable for many practical inverse problems. While invertible DeepONets [42] do not require labeled data, an extra variational inference procedure is necessary to approximate the true posterior distribution.

In this paper, we propose a novel approach to address the issues of Bayesian inverse problems, namely physics-informed invertible neural networks (PI-INN). The PI-INN establishes a bijective transformation between the parametric input and the output, which consists of the expansion coefficients of forward problem solution and Gaussian latent variables. Meanwhile, a neural basis net (NB-Net) is established to obtain the optimal spatial basis functions of the solution. The loss function of PI-INN is informed by the physics equation and constraints on the distribution of INN’s output. Notably, we introduce a new independence loss term that can be naturally incorporated with physics-informed loss terms. This loss term can fully utilize the density estimated by the INN without requiring labeled data, unlike the Maximum Mean Discrepancy (MMD) loss term in [38]. Furthermore, we theoretically prove that the PI-INN can efficiently sample from the true posterior distribution of unknown parameters when the loss function approaches zero. The method admits the following main advantages:

- Our theoretical proof shows that PI-INN can efficiently sample from the true posterior distribution of the inverse problem when the loss function approaches zero. In applications, it can provide precise estimates of posterior distributions, with comparable accuracy to time-consuming approximate Bayesian computation.
- PI-INN can provide a tractable estimation of the posterior distribution, which enables efficient sampling and high-accuracy density evaluation without requiring additional variational inference procedures [42].
- The novel independence loss term can be naturally incorporated with physics-informed loss terms based on the estimated density and is particularly advantageous for high-dimensional problems. In contrast, the MMD loss term equipped in [38, 39] is only suitable for labeled data and easily suffers from the curse of dimensionality.
- PI-INN establishes a unified learning framework for Bayesian inverse problems, which combines physics-informed learning with data-driven learning.

The remainder of this paper is organized as follows. Section 2 provides the problem statement of Bayesian inverse problems. In Section 3, the framework of our physics-informed invertible neural networks (PI-INN) is introduced, where the algorithm of training and inversion approaches with PI-INN for the physical system is described in detail. In section 4, we first present the advantage of the new loss term and then demonstrate the performance of PI-INN for solving Bayesian inverse problems through several numerical examples. Finally, some concluding remarks are given in Section 5.

2. Problem statement

Consider a steady physical system described by the following PDEs:

$$\begin{cases} \mathcal{N}(u(\mathbf{x}); \lambda(\mathbf{x})) = 0, & \mathbf{x} \in \mathcal{D}, \\ \mathcal{B}(u(\mathbf{x})) = 0, & \mathbf{x} \in \partial\mathcal{D}, \end{cases} \quad (1)$$

where \mathcal{N} denotes the general differential operator defined in the domain $\mathcal{D} \subset \mathbb{R}^d$ ($d = 1, 2$), \mathcal{B} is the boundary operator on the boundary $\partial\mathcal{D}$, $\lambda(\mathbf{x})$ represents the input property field and $u(\mathbf{x})$ denotes the solutions of the PDEs.

The corresponding inverse problem aims to recover $\lambda \in \mathbb{R}^M$ from the noisy observations $\tilde{u} \in \mathbb{R}^D$ of u at specific sensors of the domain. The observation system is defined as follows:

$$\tilde{u} = \mathcal{F}(\lambda) + \epsilon, \quad (2)$$

where \mathcal{F} is the forward operator and ϵ is the observational noise. It is assumed that ϵ follows the zero-mean Gaussian with diagonal covariance $\sigma^2 \mathbf{I}_D$. The relationship of the above variables and operator is illustrated in Fig. 1. For the Bayesian inference method, the target is to obtain samples from the posterior distribution $p(\lambda | \tilde{u})$:

$$p(\lambda | \tilde{u}) \propto p(\tilde{u} | \lambda) p(\lambda), \quad (3)$$

where $p(\lambda)$ represents the prior and $p(\tilde{u} | \lambda) \propto \exp\left(-\frac{\|\tilde{u} - \mathcal{F}(\lambda)\|^2}{2\sigma^2}\right)$ is the likelihood. The main challenge

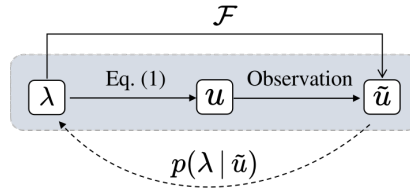


Figure 1: Graphical representation of the Bayesian inversion method.

associated with the classical Bayesian approaches lies in the computational burden of evaluating the forward model \mathcal{F} . To this end, the INN model can accurately and efficiently sample from the posterior bypass Bayes' rule, and provide rapid solutions for inversion problems in a similar problem class.

3. Methodology

3.1. Invertible neural networks

Invertible neural networks (INNs) [35, 36, 37], also known as flow-based models, are a particular type of neural network that can build bijective transformations between inputs and outputs. As shown in Fig. 2 (a), INNs build the bijection g_θ by stacking a series of reversible and differentiable coupling layers g_1, \dots, g_n , where $\Upsilon \in \mathbb{R}^F$ and $\chi \in \mathbb{R}^F$ are the random variables, $\Upsilon = g_\theta(\chi)$. The probability distributions can be expressed via the change-of-variable formula as follows:

$$\log p_\chi(\chi) = \log p_\Upsilon(g_\theta(\chi)) - \sum_{j=1}^n \log \left| \det \frac{dg_j(h_{j-1})}{dh_{j-1}} \right|, \quad (4)$$

where h_j is the intermediate variable such that $h_j = g_j(h_{j-1})$, $j = 1, \dots, n$, $h_0 = \chi$, $h_n = \Upsilon$.

In this work, we utilize the affine coupling layer as the basic building block, which was introduced in [36, 37]. Fig. 2 (b) illustrates the forward and backward operations of the affine coupling layer. In the forward

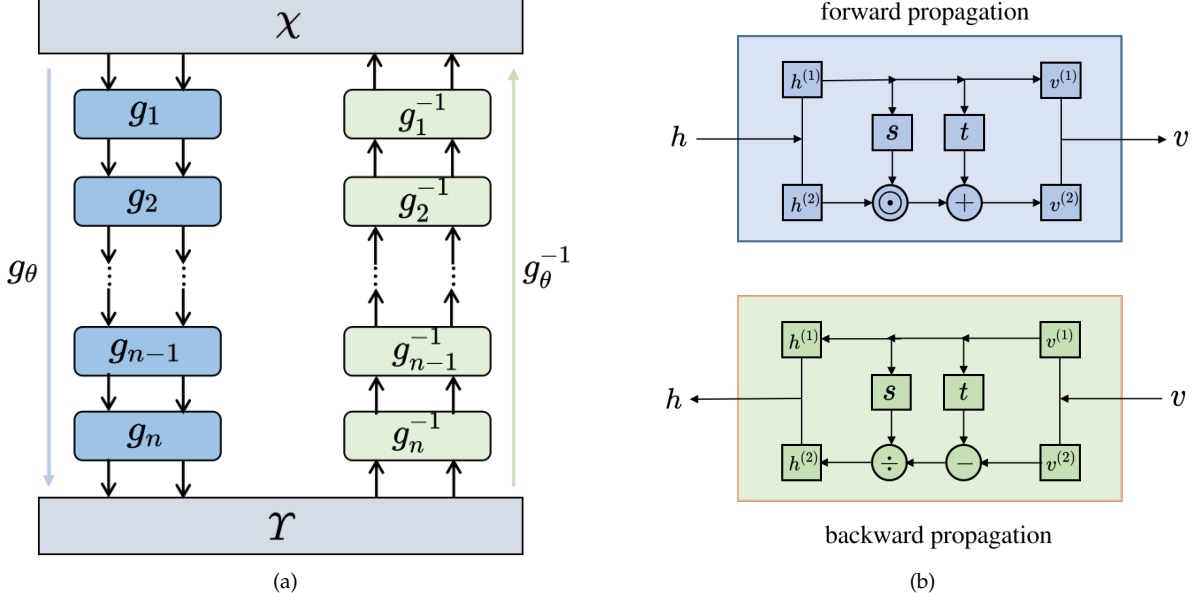


Figure 2: (a): INN with n coupling layers; (b): Illustration of affine coupling layers.

propagation, the input $h \in \mathbb{R}^F$ is first split into two parts: $h^{(1)} \in \mathbb{R}^f$ and $h^{(2)} \in \mathbb{R}^{F-f}$, $f < F$. These two parts then undergo the coupling operation as follows:

$$v^{(1)} = h^{(1)}, \quad v^{(2)} = h^{(2)} \odot \exp(s(h^{(1)})) + t(h^{(2)}), \quad (5)$$

where $s(\cdot)$ and $t(\cdot)$ are scale and translation functions respectively, and they are modeled by trainable neural networks. Here, \odot represents element-wise multiplication, and the inverse transformation can be trivially given:

$$h^{(1)} = v^{(1)}, \quad h^{(2)} = (v^{(2)} - t(v^{(1)})) \oslash \exp(-s(v^{(1)})). \quad (6)$$

The Jacobian of the forward map is given as

$$\mathbf{J} = \begin{bmatrix} \mathbb{I}_d & \mathbf{0}_{f \times (F-f)} \\ \frac{\partial v^{(2)}}{\partial h^{(1)}} & \text{diag}(\exp(s(h^{(1)}))) \end{bmatrix}. \quad (7)$$

The probability density in Eq. (4) can be easily calculated due to the diagonality of the jacobian. Then, the Jacobian of the inverse map and $\log p_z(z)$ can be calculated in the same way.

The INNs have the capacity to learn the forward mapping of a physical system and simultaneously solve inverse problems, owing to their intrinsic invertibility. However, in practical situations, inverse problems often lack unique solutions due to the information loss from measurements, which makes it impossible to establish a bijection between measurements and parameter inputs. Furthermore, the scarcity of labeled data brings difficulties to learn forward mapping. To tackle these issues, we propose physics-informed invertible neural networks (PI-INN) in the following section.

3.2. Physics-informed invertible neural networks

In this subsection, the network architecture of PI-INN is first demonstrated. As depicted in Fig. 3, PI-INN consists of two subnetworks: an invertible neural network (INN) and a neural basis net (NB-Net). Similar to DeepONets [43, 44], the separate representation of the solutions is employed by

$$u(\mathbf{x}; \lambda) = \sum_{i=1}^P c_i(\lambda) \phi_i(\mathbf{x}), \quad (8)$$

where c_i represents the expansion coefficient, and $\phi_i(x)$ is the basis function defined on the spatial domain.

The INN is designed to learn the bijective mapping between the parametric input λ and the unique pairs $[c, z]$ of expansion coefficients and random latent variables. The random latent variable z is utilized to capture the inherent information loss in the output layer, which is not contained in c . Consequently, z is assumed to be independent of c and follow a tractable probability distribution, where the uniqueness of the mapping between λ and $[c, z]$ [38] is constructed. In this work, the standard Gaussian distribution for z is adopted. Furthermore, the INN architecture consists of alternating layers and affine coupling layers. The partitioned input of the coupling layer remains unchanged for one subset, while the other subset undergoes a coupling operation. Then, the two parts of output are exchanged in alternating layers, which ensure that every dimension of the input is updated [35]. Then, a fully-connected neural network named NB-Net is employed to obtain the spatial basis functions, and the outputs of the NB-Net can be orthogonalized.

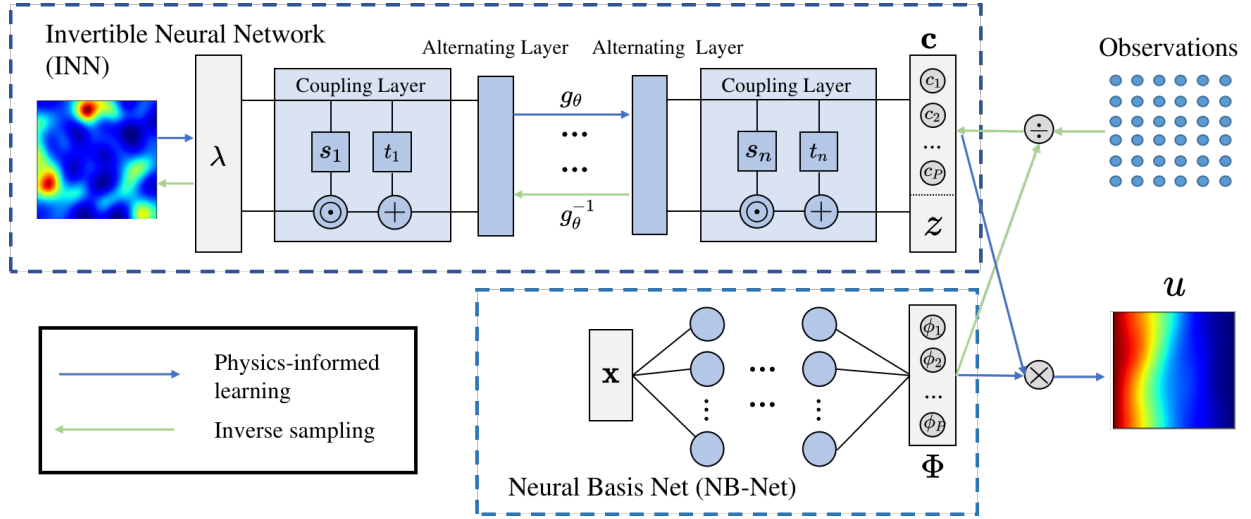


Figure 3: Schematic of PI-INN. The INN coupling with NB-Net can not only obtain the solutions of forward problems but also infer the unknown parameters from the observations. The blue and green solid lines represent the directions of learning and Bayesian inversion processes, respectively. g_θ denotes the forward map, and g_θ^{-1} is the inverse map.

It is worth highlighting that PI-INN is resolution independent, i.e., it is capable of predicting the numerical solutions at any positions of the domain \mathcal{D} and solving inverse problems with variable locations of sensors. According to Eq. (8), the vector representation of the solutions on $\{\mathbf{x}^{(i)}\}_{i=1}^M \subset \mathcal{D}$ is defined as follows:

$$\mathbf{u} = \Phi \mathbf{c}, \quad (9)$$

where

$$\Phi = \begin{bmatrix} \phi_1(\mathbf{x}^{(1)}) & \cdots & \phi_p(\mathbf{x}^{(1)}) \\ \vdots & \vdots & \vdots \\ \phi_1(\mathbf{x}^{(M)}) & \cdots & \phi_p(\mathbf{x}^{(M)}) \end{bmatrix}, \quad \mathbf{c} = \begin{bmatrix} c_1 \\ \vdots \\ c_p \end{bmatrix}, \quad \mathbf{u} = \begin{bmatrix} u(\mathbf{x}^{(1)}) \\ \vdots \\ u(\mathbf{x}^{(M)}) \end{bmatrix}.$$

Here, $\{\mathbf{x}^{(i)}\}_{i=1}^M$ is an arbitrary spatial coordinates in \mathcal{D} , and $\Phi \in \mathbb{R}^{M \times p}$ can be calculated by the NB-Net.

Given measurements $\tilde{\mathbf{u}} = [\tilde{u}(\tilde{\mathbf{x}}^{(1)}), \dots, \tilde{u}(\tilde{\mathbf{x}}^{(O)})]^T$ on $\{\tilde{\mathbf{x}}^{(i)}\}_{i=1}^O$, \mathbf{c} can be determined by solving the following optimization problem:

$$\min_{\mathbf{c}} \|\tilde{\mathbf{u}} - \tilde{\Phi} \mathbf{c}\|^2 + \rho \|\mathbf{c}\|^2, \quad (10)$$

where $[\tilde{\Phi}]_{ij} = \phi_i(\tilde{\mathbf{x}}^{(j)})$ and ρ is the regularization coefficient. Next, the training and inversion processes will be introduced by using PI-INN in the following section.

3.3. Training and inversion procedure of PI-INN

During the learning process of PI-INN (See the blue block in Fig. 3), it not only needs to learn the solutions of the forward problem but also needs to constrain the joint distribution $q(\mathbf{c}, z)$. Here, $q(\mathbf{c}, z)$ needs to satisfy

two important assumptions [38]: z must strictly follow the standard Gaussian distribution, and \mathbf{c} and z are independent of each other, i.e., $q(z|\mathbf{c}) = q(z)$. This is to prevent encoding of the same information in both \mathbf{c} and z , which will introduce more errors in the inversion process. Then, [38] utilized MMD to minimize the distance between the joint distribution of output variables given by INN and the product of the marginal distribution given by data (see Appendix C for details). While MMD can effectively distinguish between two distributions in low dimensions, it becomes less effective and requires a larger number of samples as the dimensionality increases [45]. Unlike MMD, a novel independence loss term is proposed, which does not require labeled data for \mathbf{c} , and its efficiency does not decay as the dimensionality increases. It is defined as follows

$$\mathcal{L}_{\text{ind}} = \frac{1}{N} \sum_{i=1}^N \left\| \log q(\hat{\mathbf{c}}^{(i)}, \hat{z}^{(i)}) - \log q(\hat{\mathbf{c}}^{(i)}, z^{(i)}) - (\log p(\hat{z}^{(i)}) - \log p(z^{(i)})) \right\|^2, \quad (11)$$

where $[\hat{\mathbf{c}}^{(i)}, \hat{z}^{(i)}] = g_{\theta}(\lambda^{(i)})$, $z^{(i)}$ is the sample from the standard Gaussian distribution, whereas $\hat{z}^{(i)}$ represents the output of INN for latent variables. $p(z)$ is the probability density function of the standard Gaussian distribution and $q(\mathbf{c}, z)$ is the joint distribution given by INN, which can be calculated using the change-of-variables formula. Finally, the explicit expression of the loss function is given as follows:

$$\mathcal{L} = \alpha \mathcal{L}_{\text{equ}} + \beta \mathcal{L}_{\text{bound}} + \gamma \mathcal{L}_{\text{ind}}, \quad (12)$$

where

$$\mathcal{L}_{\text{equ}} = \frac{1}{N} \sum_{i=1}^N \left\| \mathcal{N}(\hat{u}^{(i)}; \lambda^{(i)}) \right\|^2, \quad \mathcal{L}_{\text{bound}} = \frac{1}{N} \sum_{i=1}^N \left\| \mathcal{B}(\hat{u}^{(i)}) \right\|^2. \quad (13)$$

Here, \mathcal{L}_{equ} represents equation loss term, $\mathcal{L}_{\text{bound}}$ is boundary loss term, and \mathcal{L}_{ind} is independence loss term. $\hat{u}^{(i)} = \sum_{j=1}^P c_j(\lambda^{(i)})\phi_j$ is the predicted solutions of forward problem, and α, β, γ are relative weights of three loss terms. For the implementation, \mathcal{L}_{equ} can also be defined as the variational formulation (see Appendix D). Forward training optimizes the mapping $[\hat{\mathbf{c}}^{(i)}, \hat{z}^{(i)}] = g_{\theta}(\lambda^{(i)})$ and implicitly determines its inverse $\lambda^{(i)} = g_{\theta}^{-1}(\hat{\mathbf{c}}^{(i)}, \hat{z}^{(i)})$. The detailed training process is summarized in Algorithm 1.

Algorithm 1 Training procedure for PI-INN

Input: Training set: $\{\lambda^{(i)}\}_{i=1}^N$, number of epochs: E_{train} , learning rate: η , batch size: N_{batch} , loss function: L , weights of loss terms: α, β, γ , coordinates set: $\{\mathbf{x}^{(j)}\}_{j=1}^M$, number of terms in (8): N_p .

for epoch = 1 : E_{train} **do**

Sample minibatches from the training data and the latent space: $\{\lambda_i\}_{i=1}^{N_{\text{batch}}}, \{z_i\}_{i=1}^{N_{\text{batch}}}, z_i \stackrel{\text{i.i.d.}}{\sim} \mathcal{N}(0, \mathbf{I})$;

Calculate $[\hat{\mathbf{c}}^{(i)}, \hat{z}^{(i)}] = g_{\theta}(\lambda^{(i)})$; ▷ g_{θ} is the forward map of invertible neural network.

Substitute $\{\mathbf{x}^{(j)}\}_{j=1}^M$ into the NB-Net, and assemble matrix $\Phi \in \mathbb{R}^{M \times P}$;

$\hat{u}^{(i)} = \Phi \hat{\mathbf{c}}^{(i)}$;

$\mathcal{L} = L(\hat{u}^{(i)}, \hat{z}^{(i)}, z^{(i)})$;

$\nabla \theta \leftarrow \text{Backpropagation}(\mathcal{L})$;

$\theta \leftarrow \theta - \eta \nabla \theta$;

end for

Output: Trained PI-INN.

In the process of inversion, Bayesian inference can be accomplished by running the INN reversely, as shown by the green line in Fig. 3. Given the measurement \tilde{u} , the unknown input parameter can be repeatedly sampled with the latent variables z shaped as a Gaussian distribution, and \mathbf{c} keeps constant. Additionally, the desired posterior $p(\lambda | \tilde{u})$ is represented by the PI-INN, which transforms the known distribution $p(z)$ to the unknown input parameter space conditioned by different observations. We have theoretically proved that a well-trained PI-INN can efficiently sample, and explicitly provide the true posterior distribution without multiple likelihood evaluations required by classical Bayesian inversion methods (see Appendix

A). The detailed inversion procedure is illustrated in Algorithm 2.

Algorithm 2 Inversion procedure for PI-INN

Input: Trained PI-INN, locations of sensors: $\{\tilde{\mathbf{x}}^{(i)}\}_{i=1}^O$, observations: $\tilde{\mathbf{u}}$, number of inversion samples: N_{samples} , regularization parameter: ρ .

Substitute $\{\tilde{\mathbf{x}}^{(i)}\}_{i=1}^O$ into the NB-Net and assemble matrix $\tilde{\Phi} \in \mathbb{R}^{O \times N_P}$;

Calculate $\tilde{\mathbf{c}} = (\tilde{\Phi}^T \tilde{\Phi} + \rho \mathbf{I}_P)^{-1} \tilde{\Phi}^T \tilde{\mathbf{u}}$;

for $k = 1 : N_{\text{samples}}$ **do**

 Sample $z^{(k)} \sim \mathcal{N}(0, \mathbf{I})$;

 Calculate $\tilde{\lambda}^{(k)} = \mathbf{g}_{\theta}^{-1}(\tilde{\mathbf{c}}, z^{(k)})$;

end for

Output: Samples of posterior distribution: $\{\tilde{\lambda}^{(k)}\}_{k=1}^{N_{\text{samples}}}$.

Remark 3.1. Although PI-INN is designed for the purpose of being physics-informed, it can also be applied to labeled data, where a unified framework for both data-driven learning and physics-informed learning is introduced in Appendix B.

Remark 3.2. It is noted that the dimension of the input needs to be identical to the dimension of the output for the INN, i.e., $\text{ndim}(\lambda) = \text{ndim}(\mathbf{c}) + \text{ndim}(\mathbf{z})$. However, if the dimension of λ is relatively smaller than the summation of $\text{ndim}(\mathbf{c})$ and $\text{ndim}(\mathbf{z})$, the padding variable ζ may be recommended, such that the summation of $\text{ndim}(\lambda)$ and $\text{ndim}(\zeta)$ equals that of $\text{ndim}(\mathbf{c})$ and $\text{ndim}(\mathbf{z})$. In this work, $\zeta \sim \mathcal{N}(0, \mathbf{I})$ is chosen.

4. Numerical experiments

In this section, several experiments are given to confirm the effectiveness of the PI-INN model. Firstly, the performance of our independence loss term is demonstrated and compared with the MMD loss term in [38] through solving an inverse kinematics problem. Then, the PI-INN model is applied to solve the inverse problems of 1-d and 2-d diffusion equations, and the inversion results are compared with MCMC. Finally, the practical applicability of the PI-INN model is also demonstrated in the seismic traveltime tomography problem. The loss functions used for each experiment are defined in Appendix D, and the accuracy of the posterior sample can be analyzed by the L_2 relative errors defined as follows:

$$\text{Relative } L_2 \text{ error} = \frac{\|\tilde{\lambda} - \lambda\|_2}{\|\tilde{\lambda}\|_2}, \quad (14)$$

where λ and $\tilde{\lambda}$ is the predicted and reference value, respectively.

4.1. Inverse kinematics

In this subsection, the accuracy and efficiency of our independence loss term will be demonstrated by the use of the inverse kinematics problem introduced in [38], where an articulated arm moves vertically along a rail and rotates at three joints. In Fig. 4 (a), the left dotted line symbolizes the rail, and the position coordinate of the arm is denoted by x_1 , while the rotation angles of the three joints are represented by x_2 , x_3 , and x_4 . Then, the forward problem will calculate the coordinate of end point \mathbf{y} of the articulated arm, and the forward map can be defined as follows:

$$\begin{aligned} y_1 &= l_1 \cos(x_2) + l_2 \cos(x_3 - x_2) + l_3 \cos(x_4 - x_2 - x_3), \\ y_2 &= x_1 + l_1 \sin(x_2) + l_2 \sin(x_3 - x_2) + l_3 \sin(x_4 - x_2 - x_3). \end{aligned} \quad (15)$$

where $l_1 = 0.5$, $l_2 = 0.5$, and $l_3 = 1.0$ are the length of three arms. The prior of parameters are specified by normal distributions: $x_i \sim \mathcal{N}(0, \sigma_i)$, and $\sigma_1 = 0.25$, $\sigma_2 = \sigma_3 = \sigma_4 = 0.5 \hat{=} 28.65^\circ$. The inverse problem is to determine all the feasible parameters that generate the endpoint $\tilde{\mathbf{y}}$ of the arm.

To demonstrate the efficiency of the independence loss term, we trained two data-driven INN models, denoted as INN 1 and INN 2, to solve the problem (NB-Net was not utilized in this example). MMD and our independence loss terms are leveraged to constrain the output distributions of INN 1 and INN 2, respectively. The detailed loss functions are provided in [Appendix D.1](#). Here, INN 1 consists of 8 affine coupling layers, where both $s(\cdot)$ and $t(\cdot)$ contain 3 fully-connected layers with 48 neurons. INN 2 has the same architecture as INN 1 for comparison (slightly different from the architecture in [38]). For two INN models, the input and output are $x = (x_1, x_2, x_3, x_4)$ and $[y_1, y_2, z]$ with $\text{ndim}(z) = 2$, respectively. The models are trained with 4000 labeled data and a batch size of 64. The Adam optimizer is used with an initial learning rate of 5×10^{-4} and 1200 iterations, which decays with a rate of 0.8 at epochs 400, 600, and 1000.

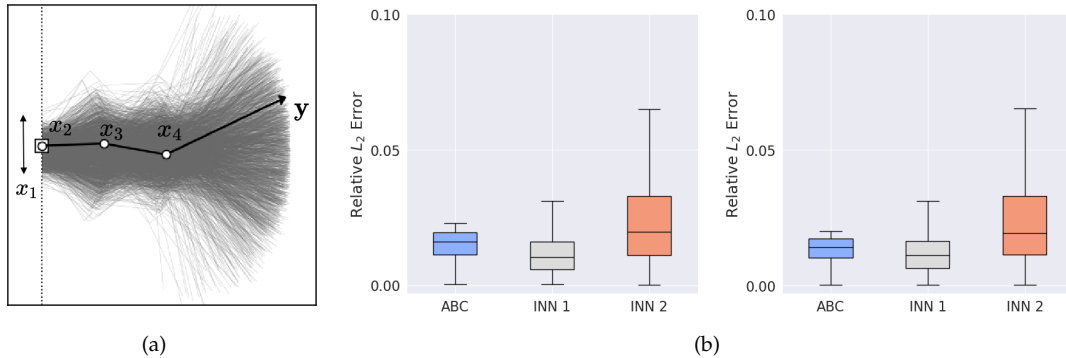


Figure 4: Inverse kinematics: (a) Articulated arm model; (b) Boxplots of relative L_2 errors of reconstructing the position of the endpoints by three methods, and the left and right figures corresponding to Test 1 and Test 2, respectively.

Then, the approximate Bayesian computation (ABC) is also used to obtain samples from the true posterior with comparison to two INN models (see more details in [Appendix D.1](#)). Fig. 4 (b) presents the boxplots of the relative L_2 errors for reconstructing the positions of the endpoints of two test cases. It can be seen that INN 1 outperforms INN 2, as it exhibits a lower mean and variance of relative errors. Moreover, the samples of posterior distributions for two test cases are displayed in Fig. 5. We observe that the sample distributions of INN 1 is similar to that of ABC, both in terms of single-parameter marginal distributions and multi-parameter joint distributions. In contrast, the sample distributions of INN 2 differ significantly from the true distribution. It is worth noting that the effectiveness of the MMD loss is contingent on the sample size [45]. It should be emphasized that much fewer training samples of 4000 data have been used for INN 1 and INN 2 in this example, which resulted in the lower efficacy of INN 2 compared to the model in [38]. Therefore, our independence loss term has demonstrated its capability in small data scenarios.

4.2. Application to 1-d diffusion equation for Gaussian and mixed Non-Gaussian random field

We consider the following diffusion equation:

$$\begin{cases} -\frac{d}{dx}\left(D(x)\frac{d}{dx}u(x)\right) = 5, & x \in [0, 1], \\ u(0) = 0, & u(1) = 1, \end{cases} \quad (16)$$

where $u(x)$ represents the concentration and $D(x)$ is the diffusion coefficient. In this example, we assume $D(x; \omega) = \exp(\tilde{D}(x; \omega))$ follows an exponential form of a Gaussian random field (GRF), where \tilde{D} is defined in Eq. (17). The Karhunen-Loève expansion (KLE) of $\tilde{D}(x; \omega)$ is used to generate samples of $D(x; \omega)$, and the finite element method (FEM) is applied to obtain reference solutions with a uniform grid and the degree of freedom $N_{\text{Dof}} = 31$. The observation data is obtained by reference solutions with noise on sparse grid points.

$$\tilde{D}(x; \omega) \sim \mathcal{GP}\left(\frac{x}{2}, \frac{9}{25}\exp\left(-\frac{\|x - x'\|_2}{2}\right)\right), \quad x, x' \in [0, 1], \quad (17)$$

We set $u(x; \lambda) = \sum_{i=1}^5 c_i(\lambda)\phi_i(x)$, where $\{\phi_1(x), \dots, \phi_5(x)\}$ will be approximated by an NB-Net with 6 hidden layers and 64 neurons. Assumed that z follows a 5-dimensional standard Gaussian distribution, and the

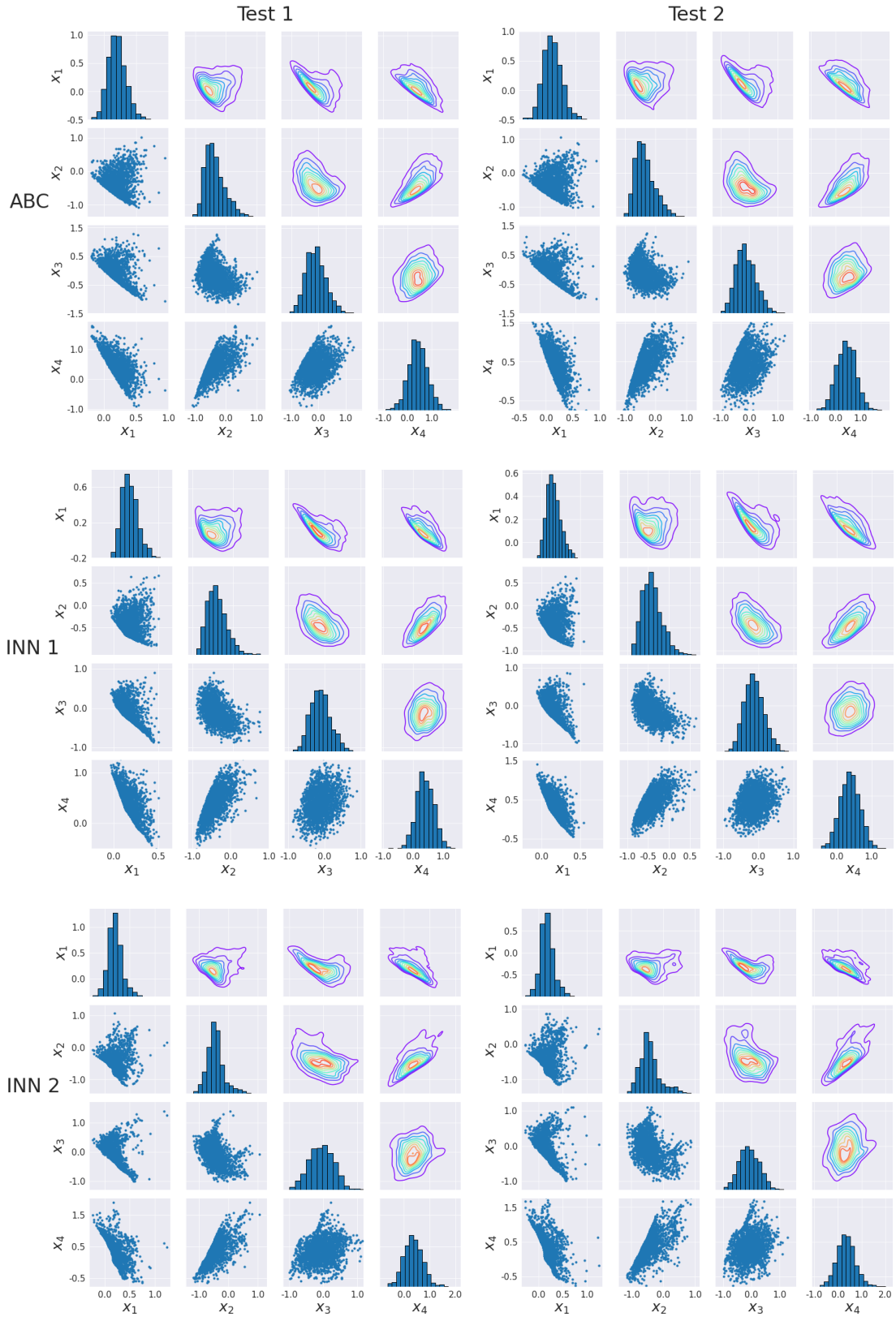


Figure 5: Inverse kinematics: Sample distributions of two test cases for ABC and two INN models. In each figure, the diagonal display the histograms of four parameters, while the lower left triangle and upper right triangle areas show the pairwise scatter diagram and density estimation of the same four parameters, respectively.

spatial coordinates $\{x^{(j)}\}_{j=1}^M$ for training are the same as the grid points for the FEM. The INN consists of 8 coupling layers, where both $s(\cdot)$ and $t(\cdot)$ have 1 hidden layer with 100 neurons and ReLU activation function. To avoid the computation of second-order derivatives, \mathcal{L}_{equ} is defined in the variational formulation. We use 4000 unlabeled data with a batch size of 64 for training and train our model for 1000 epochs using the Adam optimizer in Pytorch. The learning rate is initially set to 1×10^{-3} and decays with a rate of 0.8 at epochs 600 and 900.

To test the efficiency of our model, we obtain the posterior samples of $D(x)$ using Algorithm 2, and compare the results with those obtained from MCMC, as shown in Fig. 6. It can be observed that, for both test cases, the posterior samples of PI-INN are consistent with the reference samples obtained through the MCMC method.

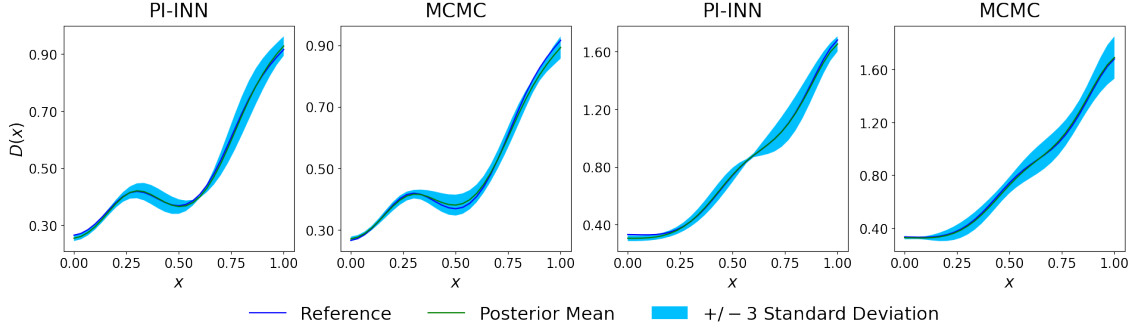


Figure 6: Two different test cases for 1-d diffusion equation under GRF prior: Comparisons of inversion results for PI-INN and MCMC, where the blue line and the green line represent the reference solution and the posterior mean, respectively. The blue shaded area is the interval of posterior mean ± 3 standard deviations with 16 evenly spaced sensors and 1% zero-mean Gaussian noise.

To further demonstrate the performance of our model, we consider the following mixed Non-Gaussian random field as the prior of $D(x)$:

$$D(x, \omega) = \exp\left(\tilde{D}(x, \omega) + \frac{4}{5}m(x, \omega)\right), \quad (18)$$

where

$$\tilde{D}(x; \omega) \sim \mathcal{GP}\left(2x(1-x), \frac{9}{25}\exp\left(-\frac{\|x-x'\|_2}{2}\right)\right), \quad x, x' \in [0, 1],$$

$$m(x, \omega) = \begin{cases} \sin\left(\frac{\pi x}{2}\right), & \text{if } \xi(\omega) \geq 0, \\ -\sin\left(\frac{\pi x}{2}\right), & \text{if } \xi(\omega) < 0. \end{cases}$$

We use the same hyperparameters for the network and training procedure as the GRF prior case. The inversion results of two test cases are displayed in Fig. 7. The posterior mean and standard deviation are in good accordance with the reference solutions from MCMC, which demonstrates the efficiency and reliability of our method.

Furthermore, the robustness of our model is validated by analyzing its performance under different combinations of measurement sensors and noise intensity. As shown in Fig. 8, we observed that the mean and standard deviation of the relative errors of the posterior samples of PI-INN has similar order of magnitudes to those of MCMC under the different observation conditions. This indicates that the performance of our model is consistent with the MCMC method, which shows the robustness and reliability of PI-INN model.

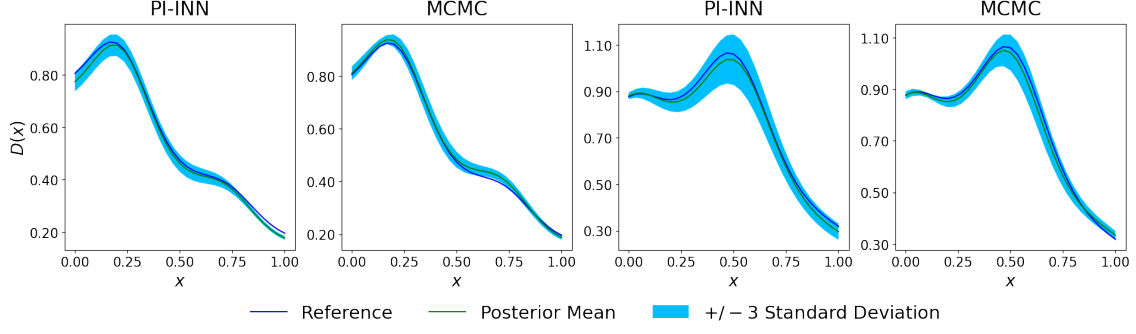


Figure 7: Two different test cases for 1-d diffusion equation under mixed Non-Gaussian prior: Comparisons of inversion results for PI-INN and MCMC, where the blue line and the green line represent the reference solution and the posterior mean, respectively. The blue shaded area is the interval of posterior mean ± 3 standard deviations with 16 evenly spaced sensors and 1% zero-mean Gaussian noise.

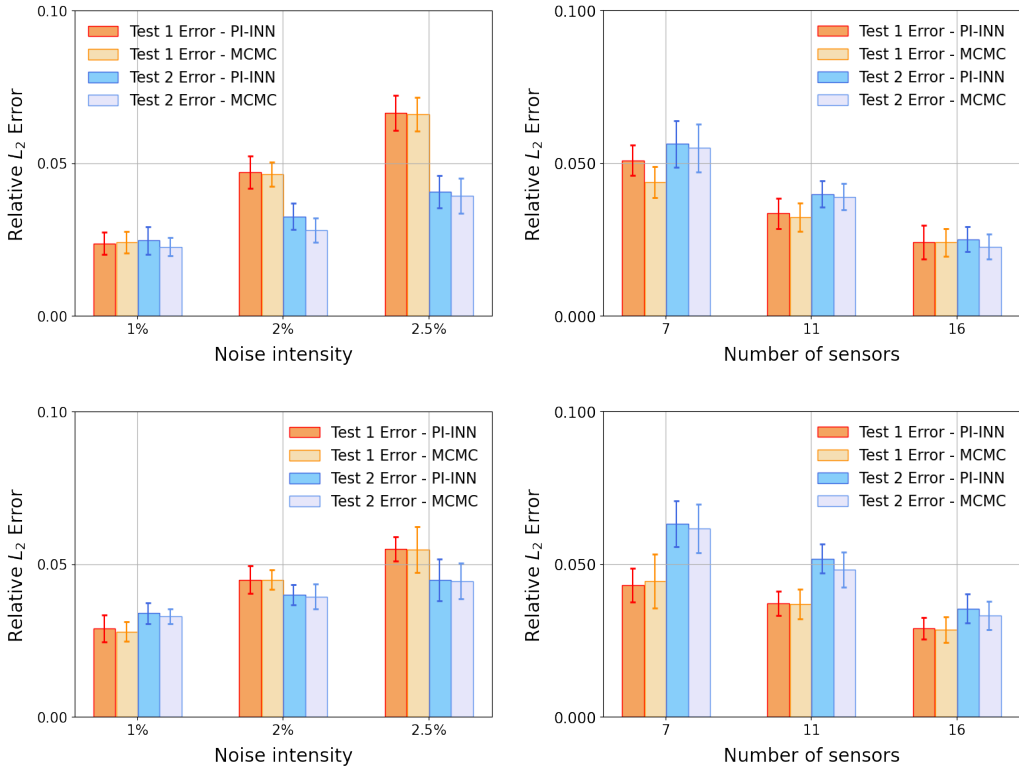


Figure 8: Relative L_2 errors of 1000 posterior samples with noise intensity and the number of sensors changed for two test cases of 1-d diffusion equation: Bars represent the averages and error bars show the standard deviations. The subfigures of the first and second row correspond to GRF and mixed Non-Gaussian random field prior cases, respectively. 16 sensors are equally spaced in $[0, 1]$ for the first column, and measurements contain 1% Gaussian noise for the second column.

4.3. Application to Darcy equation

In this example, the Darcy equation in the two-dimensional domain is considered:

$$\begin{cases} -\nabla \cdot (K(x)\nabla u(x)) = 0, & x \in [0, 1]^2, \\ u(0, x_2) = 1, u(1, x_2) = 0, \\ \frac{\partial u}{\partial n}\Big|_{x_2=0} = \frac{\partial u}{\partial n}\Big|_{y=1} = 0, \end{cases} \quad (19)$$

where $u(x)$ represents the pressure field. $K(x)$ is the permeability field, and can be sampled from $K(x, \omega) = \exp(\tilde{K}(x, \omega))$, where $\tilde{K}(x, \omega)$ is defined by Eq. (20). The domain can be divided into 64×64 uniform mesh and the reference solutions can be obtained by FEM. Several evenly spaced grid points are selected as the positions of sensors during the inversion process.

$$\tilde{K}(x, \omega) = \mathcal{GP}(0, \exp(-5\|x - x'\|_2)), \quad x, x' \in [0, 1]^2, \quad (20)$$

The random parameters of KLE are utilized as the input of INN and set $u(x; \lambda) = \sum_{i=1}^{20} c_i(\lambda)\phi_i(x)$, where the NB-Net is constructed by a fully-connected neural network with 5 hidden layers containing 128 neurons and Tanh activation function. The spatial coordinates $\{x^{(j)}\}_{j=1}^M$ for training are consistent with the grid points used for FEM. The INN consists of 8 coupling layers, where both $s(\cdot)$ and $t(\cdot)$ contain 1 hidden layer with 100 neurons and ReLU activation functions. The variational formulation of \mathcal{L}_{equ} is still adopted. 8000 unlabeled data with a batch size of 64 is utilized, and the Adam optimizer with a learning rate of 5×10^{-4} is applied to train the model for 400 iterations.

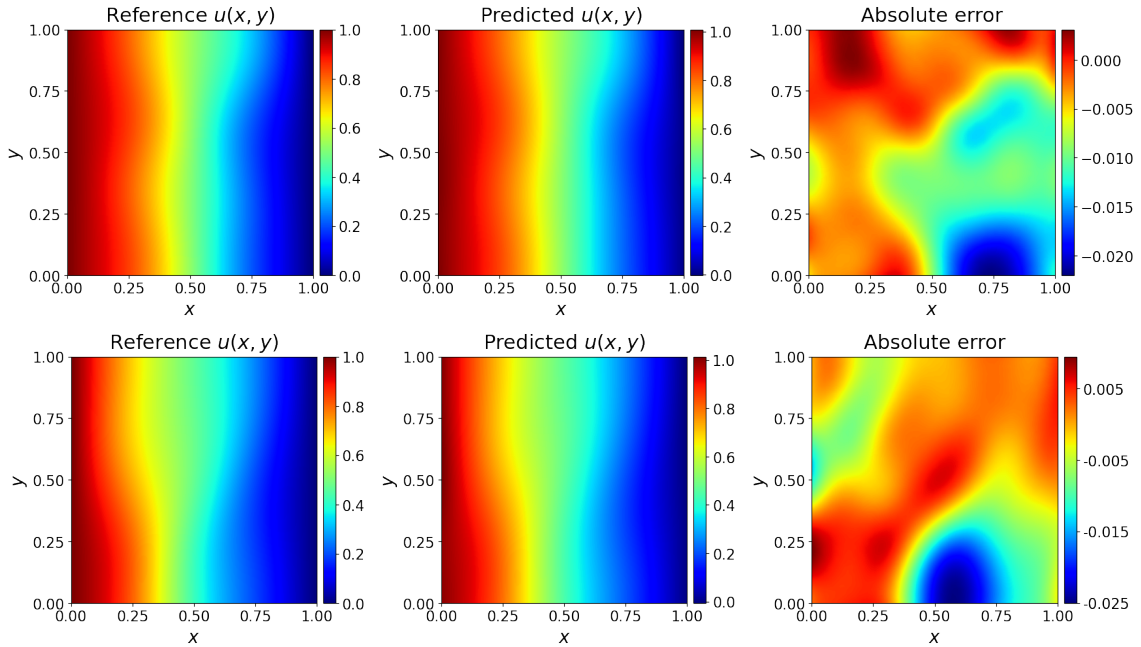


Figure 9: Comparison of the reference solutions u and the predicted solutions for 2-d Darcy equation by PI-INN model.

To assess the accuracy of our forward simulation, we display the predicted pressure fields by PI-INN for two test cases in Fig. 9. These solutions are almost identical to the reference solutions obtained by FEM, which indicates the high accuracy of our forward predictions. The comparison of inversion results for PI-INN and MCMC under two test cases are presented in Fig. 10. The posterior mean shows that both methods can effectively capture the global and local features of the true permeability fields.

To quantify the uncertainty of inversion results with the various observation conditions, we present the mean and standard deviation of the relative L_2 error of 1000 posterior samples in Fig. 11. It is noted that the mean and standard deviation of the relative errors of PI-INN is consistent with those of MCMC, which demonstrates the effectiveness of our method.

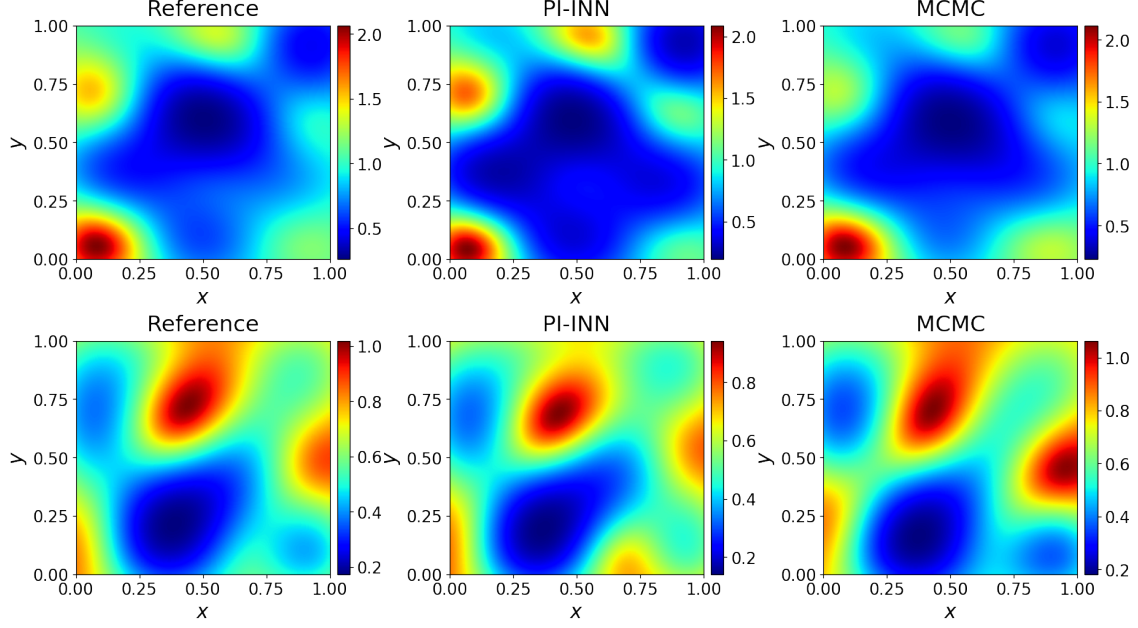


Figure 10: Comparison of the reference permeability field K and the posterior mean of PI-INN and MCMC for 2-d darcy equation. 1% noise and 22×22 sensors are used in this example.

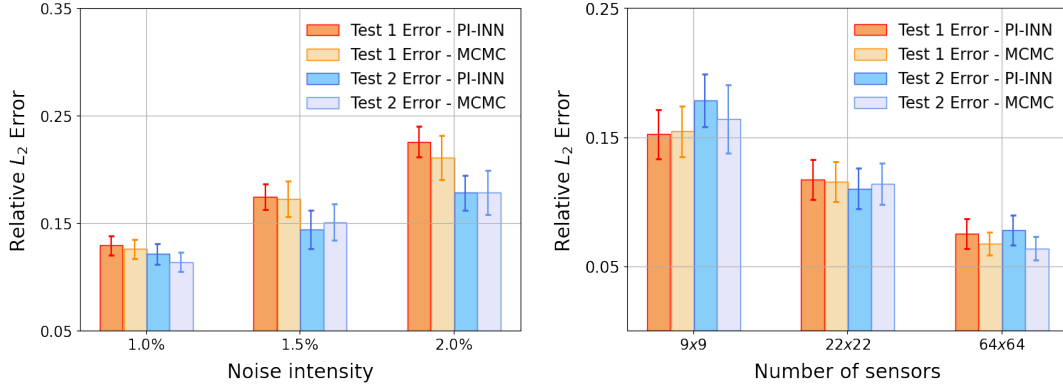


Figure 11: Relative L_2 errors of 1000 posterior samples with noise intensity and the number of sensors changed for 2-d darcy equation: Bars represent the averages and error bars show the standard deviations. 22×22 sensors and 0.5% noise are used in two subfigures, respectively.

4.4. Seismic traveltime tomography

Seismic travel time tomography is a widely used technique to image the subsurface properties and interior structures of the Earth [46]. In seismic imaging, it is typically formulated as an inverse problem to estimate underground velocity models with the observed travel time data [29]. In this example, PI-INN is applied to solve the practical seismic tomography problem based on the first-arrival travel time.

Consider the 2-d Eikonal equation defined as follows:

$$\begin{cases} |\nabla T(\mathbf{x})|^2 = \frac{1}{v^2(\mathbf{x})}, & \mathbf{x} \in \mathcal{D}, \\ T(\mathbf{x}_s) = 0, \end{cases} \quad (21)$$

where $\mathcal{D} = [0, 4]^2$ represents the domain, and $T(\mathbf{x})$ is the travel time to any position \mathbf{x} from the point-source

$\mathbf{x}_s = (2, 0)$. $v(\mathbf{x})$ is the velocity model defined on \mathcal{D} , and ∇ denotes the gradient operator. In this example, we assume that the velocity model can be parameterized as follows:

$$v(\mathbf{x}) = v(\mathbf{x}_0) + g_X(x - x_0) + g_Y(y - y_0), \quad (22)$$

where

$$g_X = 0, \quad g_Y = \begin{cases} g_Y^1, & \text{if } 0 < Y \leq h_1, \\ g_Y^2, & \text{if } h_1 < Y \leq \sum_{i=1}^2 h_i, \\ g_Y^3, & \text{if } \sum_{i=1}^2 h_i < Y \leq \sum_{i=1}^3 h_i, \\ g_Y^4, & \text{if } \sum_{i=1}^3 h_i < Y \leq \sum_{i=1}^4 h_i. \end{cases} \quad (23)$$

Here, $v(\mathbf{x}_0)$ is the velocity on the origin $\mathbf{x}_0 = (0, 0)$, g_X and g_Y are the velocity gradients along the horizontal and vertical directions, respectively. In this setting, the variation of vertical velocity gradient is determined by the depth parameters $h_i (i = 1, 2, 3, 4)$. Training data is generated with samples of the prior distributions of random parameters (such as vertical velocity gradient values and depths) in Eq. (24) and velocity models in Eq. (22). 6×6 evenly spaced sensors are distributed to record the travel time data, which is calculated using fast sweeping method [47] with 101×101 uniform mesh. The source point is fixed at $(2, 0)$.

$$\begin{aligned} g_Y^1 &\sim \mathcal{N}(0.2, 0.25), \quad g_Y^2 \sim \mathcal{N}(0.4, 0.25), \quad g_Y^3 \sim \mathcal{N}(0.5, 0.25), \quad g_Y^4 \sim \mathcal{N}(1, 1), \\ h_1 &\sim \mathcal{U}[0.75, 1.25], \quad h_2 \sim \mathcal{U}[0.75, 1.25], \quad h_3 \sim \mathcal{U}[0.75, 1.25], \quad h_4 = 4 - h_1 - h_2 - h_3, \end{aligned} \quad (24)$$

For the network architecture, the INN comprises 8 coupling layers, where both $s(\cdot)$ and $t(\cdot)$ have 1 hidden layer with 100 neurons. The NB-Net contains 6 hidden layers with 128 neurons, and the ReLU activation function is utilized for both INN and the NB-Net. Using the Adam optimizer with a learning rate of 5×10^{-4} , we train the model over $N = 4000$ unlabeled data with a batch size of 64.

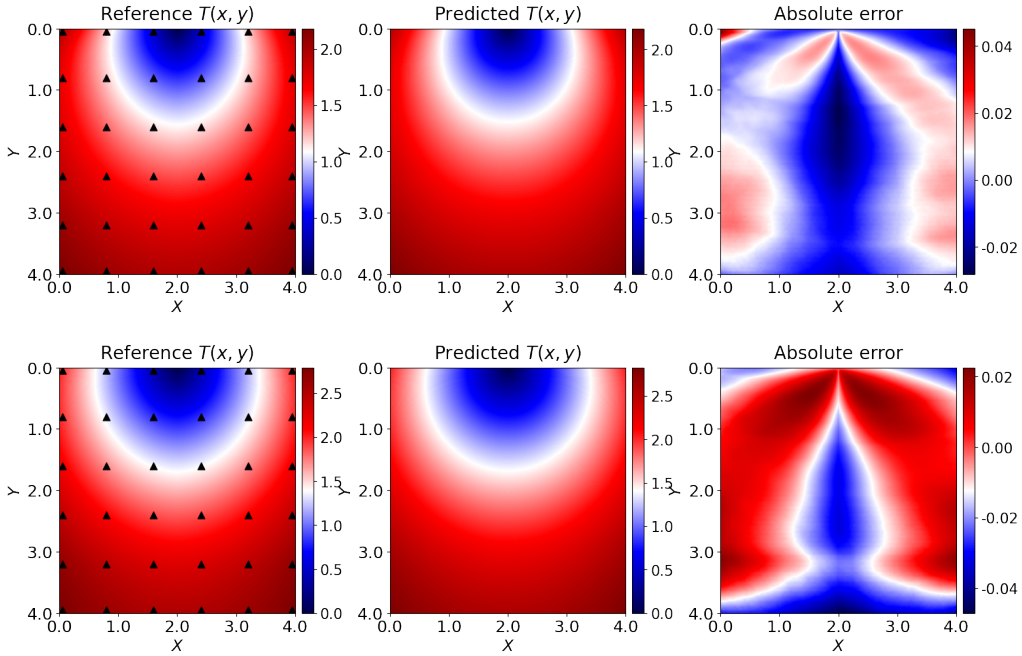


Figure 12: Comparison of the reference travel time and the predicted ones by PI-INN for two test cases of seismic traveltime tomography. The triangle marks in the first column represent the sensor locations for tomography.

As depicted in Fig. 12, the predicted travel time fields by PI-INN are almost identical to the reference

solutions, which indicates that PI-INN can provide high-accuracy forward predictions for Eq. (21). To visualize the effect of travel time tomography, the comparison of marginal posterior distributions of PI-INN and MCMC along the vertical dimension is depicted in Fig. 13. Additionally, the bivariate marginal distributions of velocities for PI-INN and MCMC at two locations (2.0, 2.52) and (2.0, 3.52) are given in Fig 14 for the two test cases. The results demonstrate that PI-INN can efficiently recover the true velocity, quantifies uncertainty, and captures correlations of velocity models. These findings highlight the potential of our PI-INN to solve practical problems in geophysical inversion.

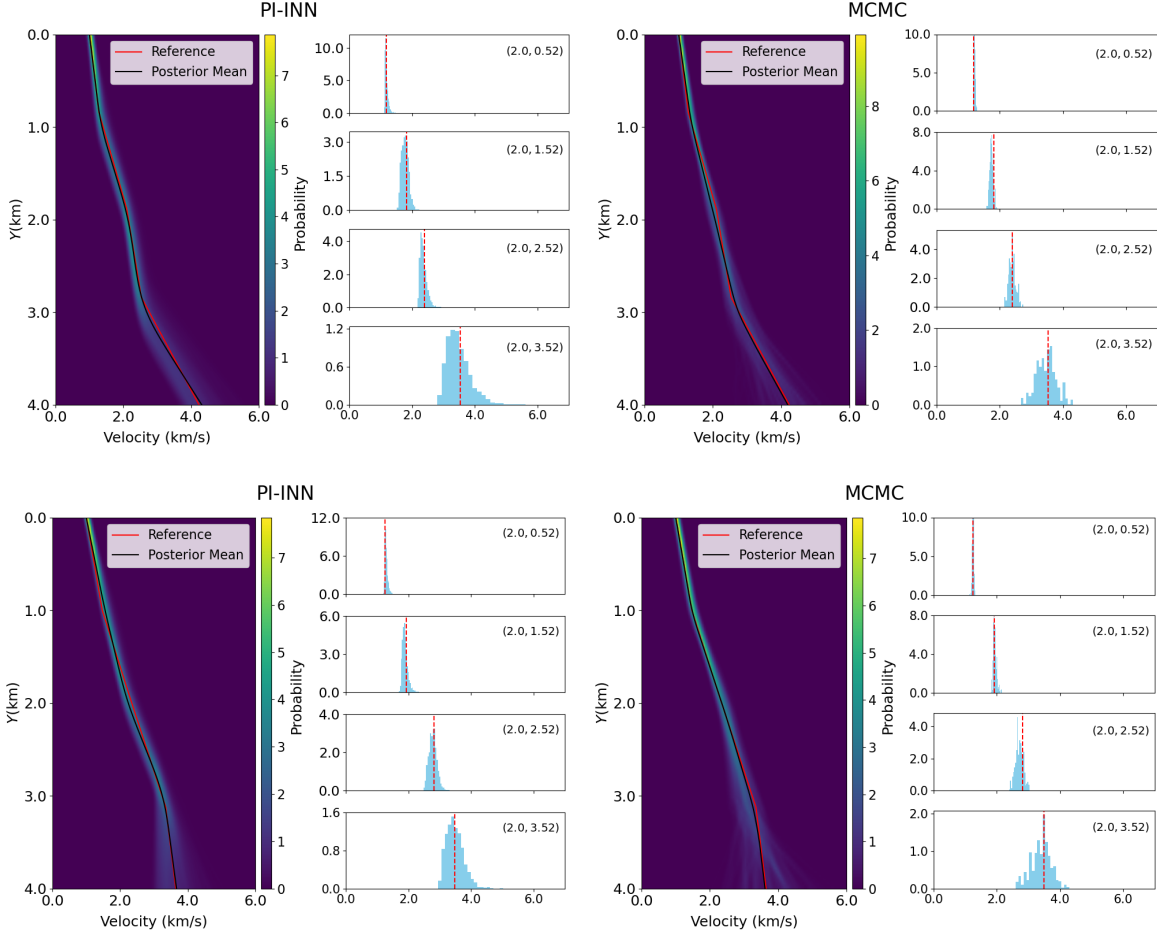


Figure 13: The marginal posterior distributions obtained using PI-INN (two left subfigures) and MCMC (two right subfigures) for test cases. 6×6 sensors and 10% noise are used in this example. Black and red lines show the reference solution and posterior mean velocity, respectively. At the right side of each panel, the marginal posterior distributions are plotted for four positions, whose coordinates have been marked in the upper right corner.

5. Conclusions

In this paper, a novel PI-INN is proposed to efficiently solve Bayesian inverse problems, which is quite general and provides a unified learning framework for Bayesian inverse problems that combines physics-informed learning with data-driven learning. In contrast to traditional Bayesian inference, PI-INN can provide a tractable estimation of the posterior distribution, which enables efficient sampling and high-accuracy density evaluation through the novel independence loss term incorporated with physics-informed loss terms and is particularly advantageous for high-dimensional problems. Moreover, the asymptotic analysis of PI-INN is theoretically derived under the assumption that the loss function approaches zero. Numerical experiments show that the proposed PI-INN is stable and effective, and can also provide enough

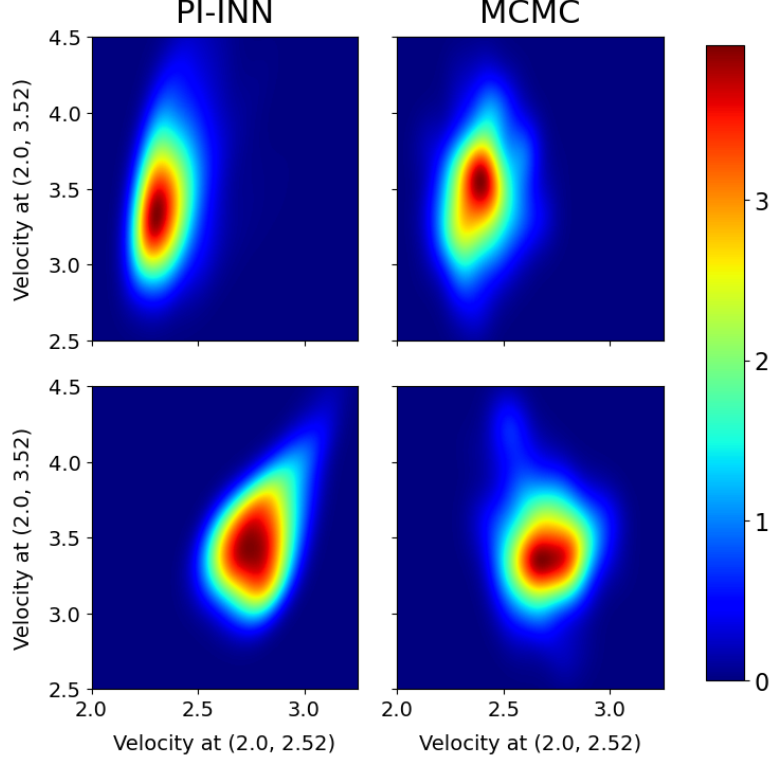


Figure 14: The bivariate marginal distributions of velocities at the locations of (2.0,2.52) and (3.0,3.52) obtained using PI-INN and MCMC, respectively, for the two velocity profiles in Fig 13.

numerical accuracy for the indirect sparse and noisy measurement data, which supports the theoretical results of this paper. Future work will focus on the various practical applications to solve Bayesian inverse problems in geophysics and Earth science.

Acknowledgement

The authors were supported by the National Science Foundation of China (Nos. 12271409 and 12171367), the Natural Science Foundation of Shanghai (No. 21ZR1465800), Shanghai Municipal Science and Technology Commission (Nos. 20JC1413500, 21JC1403700 and 2021SHZDZX0100), the Interdisciplinary Project in Ocean Research of Tongji University and the Fundamental Research Funds for the Central Universities.

Appendix A. Asymptotic analysis of PI-INN

During the training processes, the asymptotic analysis of PI-INN is given with all the loss terms \mathcal{L}_{equ} , $\mathcal{L}_{\text{bound}}$ and \mathcal{L}_{ind} in Eq. (12) approach zero when N approximate ∞ . Here, the true posterior distribution $p(\lambda | \tilde{u})$ can be sampled by Algorithm 2, where \tilde{u} is the observation data.

First of all, assuming $\mathcal{L}_{\text{ind}} = 0$, for any $z' \sim \mathcal{N}(0, I)$ and the unique pairs $[\hat{c}, \hat{z}]$, we have

$$\log q(\hat{c}, \hat{z}) - \log q(\hat{c}, z') = \log p(\hat{z}) - \log p(z'). \quad (\text{A.1})$$

Then,

$$\log \frac{q(\hat{z}|\hat{c})q(\hat{c})}{q(z'|\hat{c})q(\hat{c})} = \log \frac{p(\hat{z})}{p(z')}, \quad \Rightarrow \log \frac{q(\hat{z}|\hat{c})}{p(\hat{z})} = \log \frac{q(z'|\hat{c})}{p(z')}. \quad (\text{A.2})$$

When $[\hat{c}, \hat{z}]$ is fixed, and define $c = \log \frac{q(\hat{z}|\hat{c})}{p(\hat{z})}$, where c is the constant. Then $q(z'|\hat{c}) = cp(z')$, and

$$\int q(z'|\hat{c})dz' = \int p(z')dz' = 1, \quad \Rightarrow c = 1, \quad q(z'|\hat{c}) = p(z'). \quad (\text{A.3})$$

By the arbitrary nature of z' , $q(z|\hat{c}) = p(z)$.

Given the conditional distribution $p(\lambda|\tilde{c})$, where \tilde{c} is the corresponding expansion coefficient of \tilde{u} , and an output distribution $q(\tilde{c}, z)$ can be obtained by the trained INN. Suppose $\mathcal{L}_{\text{equ}} = \mathcal{L}_{\text{bound}} = 0$, we have $\hat{c} = \tilde{c}$, and $q(\tilde{c}) = \delta(c - \tilde{c})$, where $q(\tilde{c})$ is the output marginalized distribution for c . Then $q(\tilde{c}, z)$ satisfies the following equation:

$$q(\tilde{c}, z) = q(\tilde{c})q(z|\tilde{c}) = \delta(c - \tilde{c})p(z), \quad (\text{A.4})$$

Therefore, $q(\tilde{c}, z)$ can be sampled by fixing \tilde{c} with samples of $z \sim p(z)$. Finally, the sample of $p(\lambda|\tilde{c})$ can be obtained by inversion of INN, which is equivalent to the true posterior $p(\lambda|\tilde{u})$. This completes the proof.

Appendix B. Construction of the unified loss functions for data-driven and physics-informed INN

In certain situations, the labeled data of u corresponding to some known parameters λ may already be available. In such cases, these pre-recorded data can be leveraged to expedite the training convergence. Here, we introduce the construction of the unified loss functions for data-driven and physics-informed INN.

Given the training sets $\{\{\lambda^{(i)}, u^{(i)}\}_{i=1}^{N_l}, \{\lambda^{(i)}\}_{i=1}^{N_u}\}$, where N_l and N_u represent the number of training samples with and without labeled data, respectively. Then, the total loss function consists of two components, that is

$$\mathcal{L} = \mathcal{L}_{\text{labeled}} + \mathcal{L}_{\text{unlabeled}}. \quad (\text{B.1})$$

The first component can be written as follows

$$\mathcal{L}_{\text{labeled}} = \mathcal{L}_{\text{data}} + \mathcal{L}_{\text{l,ind}}, \quad (\text{B.2})$$

where

$$\mathcal{L}_{\text{data}} = \frac{1}{N_l} \sum_{i=1}^{N_l} \|u^{(i)} - \hat{u}^{(i)}\|^2, \quad \mathcal{L}_{\text{l,ind}} = \frac{1}{N_l} \sum_{i=1}^{N_l} \|\log q(\hat{c}^{(i)}, \hat{z}^{(i)}) - \log q(\hat{c}^{(i)}, z^{(i)}) - (\log p(\hat{z}^{(i)}) - \log p(z^{(i)}))\|^2,$$

and the second component can be written as follows

$$\mathcal{L}_{\text{unlabeled}} = \mathcal{L}_{\text{equ}} + \mathcal{L}_{\text{bound}} + \mathcal{L}_{\text{u,ind}}, \quad (\text{B.3})$$

where

$$\begin{aligned} \mathcal{L}_{\text{equ}} &= \frac{1}{N_u} \sum_{i=1}^{N_u} \|\mathcal{N}(\hat{u}^{(i)}; \lambda^{(i)})\|^2, & \mathcal{L}_{\text{bound}} &= \frac{1}{N_u} \sum_{i=1}^{N_u} \|\mathcal{B}(\hat{u}^{(i)})\|^2, \\ \mathcal{L}_{\text{u,ind}} &= \frac{1}{N_u} \sum_{i=1}^{N_u} \|\log q(\hat{c}^{(i)}, \hat{z}^{(i)}) - \log q(\hat{c}^{(i)}, z^{(i)}) - (\log p(\hat{z}^{(i)}) - \log p(z^{(i)}))\|^2. \end{aligned}$$

It is noted that the relative weights of loss terms are omitted for the sake of convenience.

Appendix C. Introduction of MMD loss term for INN

The Maximum Mean Discrepancy (MMD) is a kernel-based method used to measure the distance between two probability distributions that can only be accessed through their respective samples [48]. For instance, suppose that X and X' are random variables following the probability distribution p , and that Y and Y' are

random variables following the probability distribution q . Then the MMD can be expressed as:

$$\text{MMD}[p, q] = \mathbb{E}_{X, X'}[k(X, X')] - 2\mathbb{E}_{X, Y}[k(X, Y)] + \mathbb{E}_{Y, Y'}[k(Y, Y')],$$

where k is a kernel function. In [38], MMD is used to measure the distribution distance between $p(c)p(z)$ and $q(c, z)$ (c refers to the measurement data in [38]. Here the notation consistent with Section 3.2-3.3 is used to avoid confusion). Ardizzone et al. demonstrated that if $\text{MMD}[p(c)p(z), q(c, z)] = 0$, c and z are independent and z follows the standard Gaussian distribution. However, calculation of the MMD term requires a large amount of labeled data, which may be difficult to obtain in many practical applications [45].

Appendix D. Some details implemented for numerical experiments

Some settings of four numerical examples will be described in detail. For example 4.1, ABC method and loss functions of two INN models will be introduced. For example 4.2-4.4, we will focus on demonstrating the equation loss terms, and they share the same independence loss term.

Appendix D.1. Inverse kinematics

Appendix D.1.1. Approximate Bayesian computation (ABC)

ABC is a statistical method used for approximating the likelihood function of a Bayesian model. Instead of computing the likelihood directly, ABC simulates datasets from the model and compare them to the observed data, using a distance measure to determine how well they match. Based on the principle of rejection sampling, if the distance between the simulated and observed data is smaller than a predefined threshold, the corresponding parameter values are accepted as possible parameter values for the model.

In this example, the distance threshold is 0.035. We generate samples x from the prior distribution and select the ones where the L_2 distance between the corresponding simulated value y and the observation \tilde{y} is less than 0.035 until 2000 accepted samples are obtained.

Appendix D.1.2. Loss functions for INN models

Given training set $\{(x^{(i)}, y^{(i)})\}_{i=1}^N$, where $x = (x_1, x_2, x_3, x_4)$, $y = (y_1, y_2)$, the different loss functions are defined for two INN models as

Loss functions of INN 1:

$$\mathcal{L} = \frac{1}{N} \sum_{i=1}^N \underbrace{\alpha \|\mathbf{y}^{(i)} - \hat{\mathbf{y}}^{(i)}\|^2}_{\text{I}} + \underbrace{\beta \|\log q(\hat{\mathbf{y}}^{(i)}, \hat{z}^{(i)}) - \log q(\hat{\mathbf{y}}^{(i)}, z^{(i)}) - (\log p(\hat{z}^{(i)}) - \log p(z^{(i)}))\|^2}_{\text{II}}, \quad (\text{D.1})$$

Loss functions of INN 2:

$$\mathcal{L} = \frac{1}{N} \sum_{i=1}^N \underbrace{\alpha \|\mathbf{y}^{(i)} - \hat{\mathbf{y}}^{(i)}\|^2}_{\text{I}} + \underbrace{\beta \text{MMD}[p(\mathbf{y}^{(i)})p(z^{(i)}), q(\mathbf{y}^{(i)}, z^{(i)})]}_{\text{II}} + \underbrace{\gamma \text{MMD}[p(\mathbf{x}^{(i)}), q(\mathbf{x}^{(i)})]}_{\text{III}}, \quad (\text{D.2})$$

where α, β, γ represent the weights of different loss terms, respectively. Part I in Eqs. (D.1) and (D.1) is the forward-fitting loss term. In Eq. (D.1), II is the independence loss. In Eq. (D.2), II represents the MMD loss, and a reverse MMD loss III is added to accelerate convergence, as in [38]. The Inverse Multiquadratic $k(x, x') = 1/(1 + \|(x - x')/h\|^2)$ is used as the kernel function of MMD, where $h = 1.2$.

Appendix D.2. 1-d diffusion equation

Consider the following elliptic equation

$$-\nabla \cdot (K(\mathbf{x})\nabla u(\mathbf{x})) = f(\mathbf{x}), \mathbf{x} \in \mathcal{D},$$

and the equation loss term can be constructed with its variational form:

$$\begin{aligned}\mathcal{L}_{\text{equ}} &= \mathbb{E}_{K,c} \left[\left(-\nabla \cdot (K(\mathbf{x})\nabla u(\mathbf{x})) - f(\mathbf{x})h(\mathbf{x}, \mathbf{c}, r) \right)^2 \right] \\ &= \mathbb{E}_{K,c} \left[\left((K(\mathbf{x})\nabla u(\mathbf{x}), \nabla h(\mathbf{x}, \mathbf{c}, r)) - (f(\mathbf{x}), h(\mathbf{x}, \mathbf{c}, r)) \right)^2 \right],\end{aligned}\tag{D.3}$$

where the inner product is defined as $(f_1, f_2) \triangleq \int_{\mathcal{D}} f_1(\mathbf{x})^T f_2(\mathbf{x}) d\mathbf{x}$, and $h(\mathbf{x}, \mathbf{c}, r)$ is the test function:

$$h(\mathbf{x}, \mathbf{c}, r) = r^{-D_x} 1_{\|\mathbf{x}-\mathbf{c}\|_{\infty} \leq \frac{r}{2}},$$

where $\{\mathbf{x} \mid \|\mathbf{x} - \mathbf{c}\|_{\infty} \leq \frac{r}{2}\}$ defines a disk in \mathcal{D} , $r > 0$ is a constant, \mathbf{c} is randomly chosen in \mathcal{D} , and D_x represents the spatial dimension. It can be seen that $h(\mathbf{x}, \mathbf{c}, r)$ defines a uniform distribution in $\{\mathbf{x} \mid \|\mathbf{x} - \mathbf{c}\|_{\infty} \leq \frac{r}{2}\}$. How to obtain the unbiased estimate of \mathcal{L}_{equ} [41] will be discussed as follows:

For $D_x = 1$, then

$$\begin{aligned}(K(x)\nabla u(x), \nabla h(x, c, r)) &= r^{-1} \left(K(c - \frac{r}{2})\nabla u(c - \frac{r}{2}) - K(c + \frac{r}{2})\nabla u(c + \frac{r}{2}) \right), \\ (f(x), h(x, c, r)) &= \mathbb{E}_{x \sim h(x, c, r)} [f(x)],\end{aligned}\tag{D.4}$$

we have

- (1) For a fixed r , draw c^i ($i = 1, \dots, n$), thus $\{x \mid \|x - c^i\|_{\infty} \leq \frac{r}{2}\}$ is a subset of \mathcal{D} ,
- (2) Sample $x^i, x^i \sim h(x, c^i, r)$ ($i = 1, \dots, n$).
- (3) Given training set $\{K^{(j)}\}_{j=1}^N$, calculate

$$(K(x)\nabla u(x), \nabla h(x, c^i, r)) = r^{-1} \left(K(c^i - \frac{r}{2})\nabla u(c^i - \frac{r}{2}) - K(c^i + \frac{r}{2})\nabla u(c^i + \frac{r}{2}) \right),\tag{D.5}$$

for $j = 1, \dots, N, i = 1, \dots, n$.

- (4) Calculate the unbiased estimate of \mathcal{L}_{equ} :

$$\hat{\mathcal{L}}_{\text{equ}} = \frac{1}{nN} \sum_{j=1}^N \sum_{i=1}^n \mathcal{L}_{\text{equ}}^{(j),i}\tag{D.6}$$

where

$$\mathcal{L}_{\text{equ}}^{(j),i} = \left((K^{(j)}(x)\nabla u(x), \nabla h(x, c^i, r)) - f(x^i) \right) \cdot \left((K^{(j)}(x)\nabla u(x), \nabla h(x, c^i, r)) - f(x^i) \right).\tag{D.7}$$

Appendix D.3. 2-d Darcy equation

The equation loss term similar to Eq. (D.3) is also used for the Darcy equation. For $D_x = 2$, let $\mathbf{x} = (x_1, x_2)^T$ and $\mathbf{c} = (c_1, c_2)^T$, we have

$$\nabla h(x_1, x_2, \mathbf{c}, r) = \begin{pmatrix} r^{-2} \left(\delta(x_1 - c_1 + \frac{r}{2}) - \delta(x_1 - c_1 - \frac{r}{2}) \right) 1_{|x_2 - c_2| \leq \frac{r}{2}} \\ r^{-2} \left(\delta(x_2 - c_2 + \frac{r}{2}) - \delta(x_2 - c_2 - \frac{r}{2}) \right) 1_{|x_1 - c_1| \leq \frac{r}{2}} \end{pmatrix}\tag{D.8}$$

Then,

$$\begin{aligned}
& (K(x_1, x_2) \nabla u(x_1, x_2), \nabla h(x_1, x_2, \mathbf{c}, r)) \\
&= \int \int K(x_1, x_2) \nabla_{x_1} u(x_1, x_2) \frac{\delta(x_1 - c_1 + \frac{r}{2}) - \delta(x_1 - c_1 - \frac{r}{2})}{r^2} 1_{|x_2 - c_2| \leq \frac{r}{2}} dx_1 dx_2 \\
&+ \int \int K(x_1, x_2) \nabla_{x_2} u(x_1, x_2) \frac{\delta(x_2 - c_2 + \frac{r}{2}) - \delta(x_2 - c_2 - \frac{r}{2})}{r^2} 1_{|x_1 - c_1| \leq \frac{r}{2}} dx_1 dx_2 \\
&= \mathbb{E}_{x_2 \sim \mathcal{U}(c_2 - \frac{r}{2}, c_2 + \frac{r}{2})} \left[\frac{K(c_1 - \frac{r}{2}, x_2) \nabla_{x_1} u(c_1 - \frac{r}{2}, x_2) - K(c_1 + \frac{r}{2}, x_2) \nabla_{x_1} u(c_1 + \frac{r}{2}, x_2)}{r} \right] \\
&+ \mathbb{E}_{x_1 \sim \mathcal{U}(c_1 - \frac{r}{2}, c_1 + \frac{r}{2})} \left[\frac{K(x_1, c_2 - \frac{r}{2}) \nabla_{x_2} u(x_1, c_2 - \frac{r}{2}) - K(x_1, c_2 + \frac{r}{2}) \nabla_{x_2} u(x_1, c_2 + \frac{r}{2})}{r} \right].
\end{aligned} \tag{D.9}$$

Then, the analysis of the unbiased estimate of \mathcal{L}_{equ} can be given as follows:

- (1) For fixed r , sample $\mathbf{c}^i = (c_1^i, c_2^i)$ so that $\{\mathbf{x} \mid \|\mathbf{x} - \mathbf{c}^i\|_\infty \leq \frac{r}{2}\} \in \mathcal{D}$
- (2) Draw $x_1^i, x_1^{i'} \sim \mathcal{U}(c_1^i - \frac{r}{2}, c_1^i + \frac{r}{2})$ and $x_2^i, x_2^{i'} \sim \mathcal{U}(c_2^i - \frac{r}{2}, c_2^i + \frac{r}{2})$ for $i = 1, \dots, n$
- (3) Given training set $\{K^{(j)}\}_{j=1}^N$, calculate

$$\begin{aligned}
e^{(j),i} &= r^{-1} K^{(j)}(c_1^i - \frac{r}{2}, x_2^i) \nabla_{x_1} u(c_1^i - \frac{r}{2}, x_2^i) - r^{-1} K^{(j)}(c_1^i + \frac{r}{2}, x_2^i) \nabla_{x_1} u(c_1^i + \frac{r}{2}, x_2^i) \\
&+ r^{-1} K^{(j)}(x_1^i, c_2^i - \frac{r}{2}) \nabla_{x_2} u(x_1^i, c_2^i - \frac{r}{2}) - r^{-1} K^{(j)}(x_1^i, c_2^i + \frac{r}{2}) \nabla_{x_2} u(x_1^i, c_2^i + \frac{r}{2}) \\
&- f(x_1^i, x_2^i)
\end{aligned} \tag{D.10}$$

$$\begin{aligned}
e^{(j),i'} &= r^{-1} K^{(j)}(c_1^{i'} - \frac{r}{2}, x_2^{i'}) \nabla_{x_1} u(c_1^{i'} - \frac{r}{2}, x_2^{i'}) - r^{-1} K^{(j)}(c_1^{i'} + \frac{r}{2}, x_2^{i'}) \nabla_{x_1} u(c_1^{i'} + \frac{r}{2}, x_2^{i'}) \\
&+ r^{-1} K^{(j)}(x_1^{i'}, c_2^{i'} - \frac{r}{2}) \nabla_{x_2} u(x_1^{i'}, c_2^{i'} - \frac{r}{2}) - r^{-1} K^{(j)}(x_1^{i'}, c_2^{i'} + \frac{r}{2}) \nabla_{x_2} u(x_1^{i'}, c_2^{i'} + \frac{r}{2}) \\
&- f(x_1^{i'}, x_2^{i'})
\end{aligned} \tag{D.11}$$

for $j = 1, \dots, N, i = 1, \dots, n$.

- (4) Calculate the unbiased estimate of \mathcal{L}_{equ} :

$$\hat{\mathcal{L}}_{\text{equ}} = \frac{1}{nN} \sum_{j=1}^N \sum_{i=1}^n e^{(j),i} e^{(j),i'}. \tag{D.12}$$

Appendix D.4. 2-d seismic tomography

Considering the singularity of the single point source and substituting $T(\mathbf{x}) = T_0(\mathbf{x})\tau(\mathbf{x})$ into Eq. (21), the following factored eikonal equation will be used [49]:

$$T_0^2 |\nabla \tau|^2 + \tau^2 |\nabla T_0|^2 + 2T_0 \tau (\nabla T_0 \nabla \tau) = \frac{1}{v^2(\mathbf{x})}, \quad \tau(\mathbf{x}_s) = 1, \tag{D.13}$$

where $T_0(\mathbf{x}) = \frac{|\mathbf{x} - \mathbf{x}_s|}{v(\mathbf{x}_s)}$. Then, the equation loss can be written as the following two terms:

$$\mathcal{L}_{\text{equ}} = \mathcal{L}_{\text{factored}} + \mathcal{L}_{\text{source}}, \tag{D.14}$$

where

$$\mathcal{L}_{\text{factored}} = \frac{1}{N} \sum_{i=1}^N \left\| T_0^2 |\nabla \hat{\tau}^{(i)}|^2 + (\hat{\tau}^{(i)})^2 |\nabla T_0|^2 + 2T_0 \hat{\tau}^{(i)} (\nabla T_0 \nabla \hat{\tau}^{(i)}) - 1/(\hat{v}^{(i)})^2 \right\|^2,$$

$$\mathcal{L}_{\text{source}} = \frac{1}{N} \sum_{i=1}^N \|\hat{\tau}^{(i)} - 1\|^2,$$

where $\{\hat{v}^{(i)}\}_{i=1}^N$ is the training set, $\hat{\tau}^{(i)}$ is the prediction solutions of $\tau^{(i)}$ by PI-INN. It is noted that $\mathcal{L}_{\text{bound}}$ is not used for this example. For the dimensionality of random variables, we set $\text{ndim}(c) = 4$ and $\text{ndim}(z) = 6$. Since seven dimensional random parameters are considered for velocity models, padding variables ζ with $\text{ndim}(\zeta) = 3$ have been added.

References

- [1] T. Bodin, M. Sambridge, Seismic tomography with the reversible jump algorithm, *Geophysical Journal International* 178 (2009) 1411–1436.
- [2] K. Miya, Recent advancement of electromagnetic nondestructive inspection technology in Japan, *IEEE Transactions on Magnetics* 38 (2002) 321–326.
- [3] S. R. Arridge, Optical tomography in medical imaging, *Inverse Problems* 15 (1999) R41–R93.
- [4] H. Engl, M. Hanke, A. Neubauer, *Regularization of Inverse Problems, Mathematics and Its Applications*, Springer Netherlands, 1996.
- [5] J. T. Slagel, J. Chung, M. Chung, D. Kozak, L. Tenorio, Sampled Tikhonov regularization for large linear inverse problems, *Inverse Problems* (2019) 24.
- [6] L. Jiang, N. Ou, Multiscale model reduction method for Bayesian inverse problems of subsurface flow, *Journal of Computational and Applied Mathematics* 319 (2017) 188–209.
- [7] J. Harlim, *Data-Driven Computational Methods: Parameter and Operator Estimations*, Cambridge University Press, first edition, 2018.
- [8] J. Liu, Y. Liu, J. Sun, An inverse medium problem using Stekloff eigenvalues and a Bayesian approach, *Inverse Problems* 35 (2019) 094004.
- [9] J. Sun, Local estimators and Bayesian inverse problems with non-unique solutions, *Applied Mathematics Letters* 132 (2022) 108149.
- [10] A. Fichtner, A. Zunino, L. Gebraad, Hamiltonian Monte Carlo solution of tomographic inverse problems, *Geophysical Journal International* 216 (2019) 1344–1363.
- [11] S. Li, C. Zhang, Z. Zhang, H. Zhao, A data-driven and model-based accelerated Hamiltonian Monte Carlo method for Bayesian elliptic inverse problems (2021). ArXiv preprint, arXiv:2104.13070.
- [12] J. Wan, N. Zabaras, A Bayesian approach to multiscale inverse problems using the sequential Monte Carlo method, *Inverse Problems* 27 (2011) 105004.
- [13] A. Beskos, A. Jasra, E. A. Muzaffer, A. M. Stuart, Sequential Monte Carlo methods for Bayesian elliptic inverse problems, *Statistics and Computing* 25 (2015) 727–737.
- [14] D. Barajas-Solano, A. Tartakovsky, Approximate Bayesian model inversion for PDEs with heterogeneous and state-dependent coefficients, *Journal of Computational Physics* (2019) 247–262.
- [15] K. Yang, N. Guha, Y. Efendiev, B. K. Mallick, Bayesian and variational Bayesian approaches for flows in heterogeneous random media, *Journal of Computational Physics* 345 (2017) 275–293.

- [16] X. Zhang, A. Curtis, Seismic Tomography Using Variational Inference Methods, *Journal of Geophysical Research: Solid Earth* 125 (2020).
- [17] C. Zhang, T. Chen, Bayesian slip inversion with automatic differentiation variational inference, *Geophysical Journal International* 229 (2022) 546–565.
- [18] J. Jia, P. Li, D. Meng, Stein Variational Gradient Descent on Infinite-Dimensional Space and Applications to Statistical Inverse Problems, *SIAM Journal on Numerical Analysis* 60 (2022) 2225–2252.
- [19] K. H. Jin, M. T. McCann, E. Froustey, M. Unser, Deep Convolutional Neural Network for Inverse Problems in Imaging, *IEEE Transactions on Image Processing* 26 (2017) 4509–4522.
- [20] J. Ker, L. Wang, J. Rao, T. Lim, Deep Learning Applications in Medical Image Analysis, *IEEE Access* 6 (2018) 9375–9389.
- [21] V. Puzyrev, Deep learning electromagnetic inversion with convolutional neural networks, *Geophysical Journal International* 218 (2019) 817–832.
- [22] D. Moghadas, One-dimensional deep learning inversion of electromagnetic induction data using convolutional neural network, *Geophysical Journal International* 222 (2020) 247–259.
- [23] M. Raissi, P. Perdikaris, G. Karniadakis, Physics-informed neural networks: A deep learning framework for solving forward and inverse problems involving nonlinear partial differential equations, *Journal of Computational Physics* 378 (2019) 686–707.
- [24] D. Zhang, L. Lu, L. Guo, G. E. Karniadakis, Quantifying total uncertainty in physics-informed neural networks for solving forward and inverse stochastic problems, *Journal of Computational Physics* 397 (2019) 108850.
- [25] E. Haghighat, M. Raissi, A. Moure, H. Gomez, R. Juanes, A physics-informed deep learning framework for inversion and surrogate modeling in solid mechanics, *Computer Methods in Applied Mechanics and Engineering* 379 (2021) 113741.
- [26] L. Lu, X. Meng, Z. Mao, G. E. Karniadakis, DeepXDE: A Deep Learning Library for Solving Differential Equations, *SIAM Review* 63 (2021) 208–228.
- [27] L. Yang, X. Meng, G. E. Karniadakis, B-PINNs: Bayesian physics-informed neural networks for forward and inverse PDE problems with noisy data, *Journal of Computational Physics* 425 (2021) 109913.
- [28] Y. Yang, P. Perdikaris, Adversarial uncertainty quantification in physics-informed neural networks, *Journal of Computational Physics* 394 (2019) 136–152.
- [29] U. bin Waheed, T. Alkhalifah, E. Haghighat, C. Song, J. Virieux, PINNtomo: Seismic tomography using physics-informed neural networks (2021). ArXiv preprint, arXiv:2104.01588.
- [30] C. Song, T. A. Alkhalifah, Wavefield Reconstruction Inversion via Physics-Informed Neural Networks, *IEEE Transactions on Geoscience and Remote Sensing* 60 (2022) 1–12.
- [31] L. Yuan, Y.-Q. Ni, X.-Y. Deng, S. Hao, A-PINN: Auxiliary physics informed neural networks for forward and inverse problems of nonlinear integro-differential equations, *Journal of Computational Physics* 462 (2022) 111260.
- [32] Y. Li, Y. Wang, L. Yan, Surrogate modeling for Bayesian inverse problems based on physics-informed neural networks, *Journal of Computational Physics* 475 (2023) 111841.
- [33] I. J. Goodfellow, J. Pouget-Abadie, M. Mirza, B. Xu, D. Warde-Farley, S. Ozair, A. Courville, Y. Bengio, Generative Adversarial Networks (2014). ArXiv preprint, arXiv:1406.2661.
- [34] D. P. Kingma, M. Welling, Auto-Encoding Variational Bayes (2022). ArXiv preprint, arXiv:1312.6114.

- [35] L. Dinh, D. Krueger, Y. Bengio, NICE: Non-linear Independent Components Estimation (2015). ArXiv preprint, arXiv:1410.8516.
- [36] L. Dinh, J. Sohl-Dickstein, S. Bengio, Density estimation using Real NVP (2017). ArXiv preprint, arXiv:1605.08803.
- [37] D. P. Kingma, P. Dhariwal, Glow: Generative Flow with Invertible 1x1 Convolutions (2018). ArXiv preprint, arXiv:1807.03039.
- [38] L. Ardizzone, J. Kruse, S. Wirkert, D. Rahner, E. W. Pellegrini, R. S. Klessen, L. Maier-Hein, C. Rother, U. Köthe, Analyzing Inverse Problems with Invertible Neural Networks (2019). ArXiv preprint, arXiv:1808.04730.
- [39] X. Zhang, A. Curtis, Bayesian Geophysical Inversion Using Invertible Neural Networks, *Journal of Geophysical Research: Solid Earth* 126 (2021).
- [40] G. Anantha Padmanabha, N. Zabarar, Solving inverse problems using conditional invertible neural networks, *Journal of Computational Physics* 433 (2021) 110194.
- [41] L. Guo, H. Wu, T. Zhou, Normalizing field flows: Solving forward and inverse stochastic differential equations using physics-informed flow models, *Journal of Computational Physics* 461 (2022) 111202.
- [42] S. Kaltenbach, P. Perdikaris, P.-S. Koutsourelakis, Semi-supervised invertible neural operators for Bayesian inverse problems, *Computational Mechanics* (2023).
- [43] L. Lu, P. Jin, G. Pang, Z. Zhang, G. E. Karniadakis, Learning nonlinear operators via DeepONet based on the universal approximation theorem of operators, *Nature Machine Intelligence* 3 (2021) 218–229.
- [44] S. Wang, H. Wang, P. Perdikaris, Learning the solution operator of parametric partial differential equations with physics-informed deepnets, *Science Advances* 7 (2021) eabi8605.
- [45] A. Ramdas, S. Jakkam Reddi, B. Poczos, A. Singh, L. Wasserman, On the Decreasing Power of Kernel and Distance Based Nonparametric Hypothesis Tests in High Dimensions, *Proceedings of the AAAI Conference on Artificial Intelligence* 29 (2015).
- [46] X. Zhao, A. Curtis, X. Zhang, Bayesian seismic tomography using normalizing flows, *Geophysical Journal International* 228 (2021) 213–239.
- [47] H. Zhao, A fast sweeping method for Eikonal equations, *Mathematics of Computation* 74 (2004) 603–627.
- [48] A. Gretton, K. M. Borgwardt, M. J. Rasch, B. Schölkopf, A. Smola, A kernel two-sample test, *J. Mach. Learn. Res.* 13 (2012) 723–773.
- [49] S. Fomel, S. Luo, H. Zhao, Fast sweeping method for the factored eikonal equation, *Journal of Computational Physics* 228 (2009) 6440–6455.